Crystallographic and mechanical investigation of intergranular stress corrosion crack initiation in austenitic stainless steel

Crystallographic and mechanical investigation of intergranular stress corrosion crack initiation in austenitic stainless steel

Tomoyuki Fujii[*1], Keiichiro Tohgo[2], Yota Mori[3], Yutaro Miura[4], and Yoshinobu Shimamura[5]

*1 Corresponding author
Department of Mechanical Engineering, Shizuoka University
3-5-1, Johoku, Naka-ku, Hamamatsu 432-8561, Japan
e-mail: fujii.tomoyuki@shizuoka.ac.jp
Tel & Fax: +81-53-478-1029

2 Department of Mechanical Engineering, Shizuoka University
3-5-1, Johoku, Naka-ku, Hamamatsu 432-8561, Japan
e-mail: tohgo.keiichiro@shizuoka.ac.jp

3 Department of Mechanical Engineering, Shizuoka University
3-5-1, Johoku, Naka-ku, Hamamatsu 432-8561, Japan
e-mail: pi.cm.knm@gmail.com

4 Department of Mechanical Engineering, Shizuoka University
3-5-1, Johoku, Naka-ku, Hamamatsu 432-8561, Japan
e-mail: balius.k2w5s0k@gmail.com

5 Department of Mechanical Engineering, Shizuoka University
3-5-1, Johoku, Naka-ku, Hamamatsu 432-8561, Japan
e-mail: shimamura.yoshinobu@shizuoka.ac.jp

Abstract

This study used crystallographic and mechanical analyses to investigate the nucleation of intergranular stress corrosion cracking (IGSCC) on a smooth surface of type 304 austenitic stainless steel. Constant load testing was conducted on thermally sensitized austenitic stainless steel in a tetrathionate solution, and the nucleation behavior of IGSCC on a smooth surface was observed in situ. Then, grain boundaries (GBs) at which stress corrosion cracks occurred were characterized based on the coincidence site lattice model, GB length, and stress acting on GBs. It was found that GBs with the following characteristics exhibited high susceptibility to IGSCC: GBs with little resistance to intergranular corrosion (IGC), long GBs, and GBs subjected to high normal stress. Shear stress acting on GBs seemed to have little effect on the nucleation of IGSCC. Then, a criterion for intergranular stress corrosion crack initiation was developed using the susceptibility of GBs to IGC, GB length, and the stresses acting on GBs.

Keywords: Intergranular stress corrosion cracking; Stress; Grain boundary; Grain boundary structure; Coincidence site lattice

1. Introduction

Austenitic stainless steel is a steel alloy containing chromium and nickel [1] that exhibits high corrosion resistance and high mechanical performance at low to high temperatures. This alloy has been used for many applications, especially structural components in chemical plants and nuclear power plants. However, many instances of corrosion and stress corrosion cracking (SCC) in austenitic stainless steel used in these plants have been reported [2, 3]. One of the reasons for SCC is so-called sensitization, which is the formation of chromium carbides along the grain boundaries (GBs) in this steel [4, 5]. Thus, the service life of structural components made of austenitic stainless steel should be evaluated with consideration of material degradation by intergranular corrosion (IGC) and intergranular SCC (IGSCC).

Many studies have used the coincidence site lattice (CSL) model to investigate IGC in austenitic stainless steels. The structure of GBs is characterized by the Σ value, which is defined as the reciprocal of the density of coincidence sites [6]. Shimada et al. [7] discussed the influence of GB character (Σ value) on IGC in type 304 stainless steel and proposed a technique to form its microstructure with high resistance to IGC. Hu et al. [8], Kobayashi et al. [9], and Barr et al. [10] also proposed techniques to improve the resistance to IGC by controlling GB networks in austenitic stainless steel. Haruna et al. [11] pointed out some uncertainties of electron backscatter diffraction (EBSD) analysis and discussed susceptibility to IGC based on the actual GB structure of Σ3 boundaries in type 304 stainless steel. Fujii et al. [12] also investigated the relationship between susceptibility to IGC and GB structure based on the width of a corroded groove as a measure of IGC susceptibility. Figure 1 shows the susceptibility (normalized IGC width) as a function of GB structure; the figure reveals that some GBs exhibit high resistance to IGC.

Many studies have also investigated IGSCC in austenitic stainless steels. SCC behavior involves multiple processes ranging from the micro to macro scale, and it has been generally discussed as two separate processes, SCC nucleation (micro-scale) and SCC growth (macro-scale). SCC growth from a long crack has been characterized by fracture mechanics parameters, such as the stress intensity factor K and J integral. Andresen and Morra [13], Terauchi et al. [14] and Fujii et al. [15] investigated the SCC growth behaviors in austenitic stainless steels, and formulated the relations between SCC growth rate and fracture mechanics parameters (da/dt-K or da/dt-J relations). Saito and

Kuniya [16] and Shoji et al. [17] developed theoretical equations to evaluate the stress corrosion crack growth based on a slip/dissolution-oxidation mechanism. Furthermore, in recent years, the effect of the gradient of stress intensity factor (dK/da) on SCC growth was pointed out by several researchers [18-20]. This fracture mechanics approach can accurately evaluate the growth rate of a long stress corrosion crack. In applications such as nuclear power plants, the remaining service life of components is evaluated based on SCC growth from a millimeter-sized crack detected during periodic inspection to final failure. On the other hand, the evaluation of SCC nucleation on a smooth surface remains controversial because the nucleation seems to be a stochastic process, and it is difficult to detect micro-cracks at the early stage of SCC. Hence, the nucleation has been statistically discussed, for example, on the basis of the CLS model using the Σ boundary, crystal misorientation at GBs, and stresses acting on GBs. Gertsman et al. [21] evaluated the susceptibility of GBs to SCC and pointed out that it was difficult to investigate the resistance of GBs to SCC using the CLS model because SCC occurred at some lower-Σ boundaries, including the Σ3 boundary, in stainless alloys. West and Was [22] investigated initiation of IGSCC from the viewpoint of normal stress acting on GBs in sensitized type 304 stainless steel. They developed the Schmid-modified grain boundary stress (SMGBS) model, in which normal stress acting on GBs is calculated using the Schmid factors of neighboring grains, and pointed out that IGSCC tended to start at GBs subjected to high normal stress. Then, West and Was [23] investigated the initiation of intergranular stress corrosion cracks from the viewpoint of strain incompatibilities at GBs in irradiated type 316L stainless steel. Stratulat et al. [24] also discussed the initiation of IGSCC based on the normal stress calculated by the SMGBS model, and concluded that the initiation site coincided with the most highly stressed GBs. Liu et al. [25] pointed out that twin- or twin-related boundaries exhibited high resistance to IGSCC, and intergranular cracks were initiated and propagated in such a way as to avoid these IGSCC-resistant GBs in type 316 stainless steel. Although SCC occurs under the conjoint action of material and tensile stress in a corrosive environment [26], these studies focused on each influencing factor independently. To develop a criterion for initiation of IGSCC, the factors that influence SCC must be considered simultaneously. Moreover, the nucleation process of SCC, which dominates the duration of the overall SCC process, needs to be clarified to evaluate total SCC life.

In this study, to clarify the nucleation of IGSCC on a smooth surface of type 304 stainless steel, constant load testing was carried out in a tetrathionate solution. Prior to SCC testing, crystal orientations on the specimen surface were measured with a scanning electron microscope (SEM) with an EBSD apparatus. Tensile load corresponding to the given tensile strain was applied in the solution, and then SCC testing was started. The behavior of intergranular crack initiation and growth was observed in-situ with an optical microscope (OM). After testing, a criterion for initiation of IGSCC was developed based on the susceptibility of GBs to IGC, the length of GBs, and the stresses acting on GBs.

2. Experimental procedure

2.1 Material, specimen, and environment

Type 304 austenitic stainless steel was used. Tables 1 and 2 show the chemical composition and mechanical properties of the steel, respectively. The steel was solutionized by heat treatment applied at 1100°C for 1 h, and then it was sensitized at 700°C for 2 h and 500°C for 24 h. The average grain size of the steel was determined as 119 μm by the line-intercept method (Japanese Industry Standard (JIS) G 0551), and the reactivation ratio of the steel was determined as 29.3% by the electrochemical reactivation method (JIS G 0580). The steel used was the same as that used in our previous study [12]. Figure 2 shows that the microstructure of the steel, which was etched using oxalic acid, displayed deeply etched GBs.

Tensile specimens were machined from the bulk steel after heat treatment. Figure 3 shows the dimensions of each tensile specimen, which had a 2×2 mm square observation area (white area in the figure). Prior to testing, the surface of the observation area was ground with emery paper up to #2000 and polished with diamond paste having 3-μm grain diameter. A strain gauge was attached to the back surface of the observation area.

SCC testing was performed in a 1% tetrathionate solution, to which sulfuric acid was added to reduce its pH to 3.0. This combination of material and solution produced accelerated testing.

2.2 SCC testing apparatus

Figure 4 shows the laboratory tensile testing apparatus with a load cell. The specimen was mounted inside a polycarbonate tube to immerse only the specimen in the corrosive solution, and constant tensile load was applied with a bolt, nut, and compressive spring. The SCC behavior was observed in situ through a glass plate with an OM (camera MS-200 and lens MS-Z420, Asahi Kogaku Manuf. Co., Ltd.). Note that the OM was positioned laterally to avoid image blurring due to bubbles and dust in the solution.

2.3 Experimental conditions

Many slip lines are observed on a specimen surface when it is plastically deformed. In preliminary testing, because the specimen was subjected to tensile loading beyond the yield stress, the initiation of grain-sized cracks could not be clearly detected because the specimen surface was too rough due to the many slip lines. Hence, the displacement corresponding to an initial given strain was applied in two steps in this study, as shown in Fig. 5. In the first step, a load corresponding to a pre-strain of 80% of the given initial strain was applied. After unloading, the observation area was polished with diamond paste and colloidal silica (OP-U, Marumoto Struers K.K.) to remove deep slip lines. In the second step, a load corresponding to the remaining strain was applied, and the total strain became the initial strain for observation. As a result, the initiation of grain-sized cracks could be detected on the relatively smooth surface of the specimen because only shallow slip lines were formed when the remaining strain was applied. During testing, the strain increased slightly due to cracking and creep.

The initial strain was set to 2.0%. In the first step, a pre-strain of 1.6% was loaded and unloaded, and the observation area surface was polished. Then, the crystal orientation of the observation area was analyzed, as described in Sec. 2.4. All surfaces except for the observation area were coated with plastic for corrosion insulation (shaded area in Fig. 3). After the specimen was mounted in the testing apparatus, the corrosive solution was poured into the tube, the remaining strain was applied to the specimen in the solution, and SCC testing was started. During testing, a constant load was maintained and the corrosive solution was changed every 12 h. The crack formation process was observed with the OM and recorded every 5 min. After testing, the specimen was cleaned with acetone to remove the plastic coating and observed with a SEM (VE-9800,

Keyence), and the crack site, crack length, and number of cracks were recorded. Three specimens were tested in this way.

2.4 Crystallography

Crystal orientation in the steel was measured with a field-emission SEM (JSM-7001F, JEOL Ltd.) with an EBSD system (TSL Solutions). The crystal orientation was analyzed with the OIM data collection and analysis (TexSEM).

To determine the influence of GB structure on susceptibility to IGSCC, GBs were classified as low-angle (misorientation angle between 5° and 15°) or large-angle (misorientation angle > 15°). Moreover, large-angle GBs were subclassified as being CSL or random boundaries. In this study, GBs that exhibited structures Σ3 to Σ29 were identified as CSL boundaries, and other large-angle GBs were regarded as random boundaries. The tolerance angle $\Delta\theta$ was used based on the Brandon criterion [27] to determine the CSL boundaries:

$$\Delta\theta = 15\Sigma^{-\frac{1}{2}} \quad . \tag{1}$$

This classification system was the same as that used in our previous study [12]. The length of GBs was determined based on the reconstructed boundaries, in which a line was drawn between two triple junctions to fit it to a set of grain boundary segments. The conditions of EBSD measurement are listed in Table 3.

2.5 Modeling of GB stresses

Microscopic stresses nonuniformly distribute within a polycrystalline material due to the elastic and plastic anisotropy of each grain comprising the material. To characterize intergranular crack initiation from a mechanical viewpoint, stresses acting on GBs should be calculated with the consideration of these anisotropic effects. In this study, the stresses were calculated based on the SMGBS model proposed by West and Was [22, 23]. The SMGBS model accounts for the combined effects of the GB plane geometry and grain orientations based on the Schmid factors of adjacent grains. A brief description of the model follows.

Figure 6 is a schematic illustration of the geometry of a GB consisting of two grains, Grains A and B, with Schmid factors of m_A and m_B, respectively. Here, we focus on the deformation of Grain A. When Grain A is plastically deformed, the normal stress σ_N acting on the GB is described as

$$\sigma_N = \sigma_{fg}^A \left(\cos\alpha\right)^2, \tag{2}$$

where σ_{fg}^A is the flow stress of Grain A and α is an angle inclined to the tensile direction based on the GB trace angle θ and tilt angle ϕ,

$$\alpha = \arccos\left(\cot^2\phi + \cot^2\theta + 1\right)^{1/2}. \tag{3}$$

According to the Schmid's law [28], a grain plastically deforms when the resolved shear stress acting on a slip system reaches the critical resolved shear stress τ_{CRSS}. Then, the yield stress σ_{yg}^A of Grain A can be described as

$$\sigma_{yg}^A = \frac{\tau_{CRSS}}{m_A}. \tag{4}$$

An elastic–perfectly plastic body is assumed in this model. To consider the effect of microstructure in a polycrystalline material, the flow stress σ_f and yield stress σ_y of the material are equal and proportional to average Schmid factor m_{ave} of the polycrystalline material,

$$\sigma_f = \sigma_y \propto \frac{1}{m_{ave}}. \tag{5}$$

By considering both eqs. (4) and (5), the flow stress of Grain A may be calculated as

$$\sigma_{fg}^A = \sigma_f \frac{m_{ave}}{m_A}. \tag{6}$$

Hence, the normal stress on the GB is calculated using eqs. (2) and (6) as

$$\sigma_N = \sigma_f \frac{m_{ave}}{m_A}\left(\cos\alpha\right)^2. \tag{7}$$

By assuming that the stress acting on the GB depends on the average flow stress of adjacent grains (Grains A and B in this case), the effective normal stress acting on the GB may be obtained as

$$\sigma_{\mathrm{N}} = \frac{\sigma_{\mathrm{f}}}{2}\left(\frac{m_{\mathrm{ave}}}{m_{\mathrm{A}}} + \frac{m_{\mathrm{ave}}}{m_{\mathrm{B}}}\right)\left(\cos\alpha\right)^2. \tag{8}$$

Similar to the effective normal stress, the effective shear stress acting on the GB described as

$$\tau_{\mathrm{N}} = \frac{\sigma_{\mathrm{f}}}{2}\left(\frac{m_{\mathrm{ave}}}{m_{\mathrm{A}}} + \frac{m_{\mathrm{ave}}}{m_{\mathrm{B}}}\right)\cos\alpha\sin\alpha. \tag{9}$$

When we applied this model in this study, some assumptions were necessary. Although we used a strain-hardening steel, the steel flow stress σ_{f} was assumed to have a 0.2% offset stress. The tilt angle ϕ was assumed to be 90° because it could not be measured by nondestructive surface observation.

3. Results and discussion

3.1 Crack initiation and propagation

Figure 7 shows the behavior of crack initiation and propagation on the specimen surface during testing, and Fig. 8 schematically illustrates the behavior shown in Fig. 7. Cracks several tens of micrometers long were first observed at a testing time of 145 min, which established an incubation period of 140-145 min. Then, the micro-crack initiation continued, and the cracks lengthened due to crack coalescence and growth. At a testing time of 720 min, we observed several cracks several hundred micrometers long and more cracks several tens of micrometers long. The crack initiation and growth stopped, and the test was terminated at a testing time of 4920 min (82 h). These same processes were observed in the other specimens.

Figure 9 shows SEM micrographs of the specimen surface after testing, which correspond to the cracks illustrated in Fig. 8(d). This figure confirms that the cracks observed by optical microscopy are real. The cracks several hundred micrometers long were deflected, and they would grow along GBs and/or coalesce from multiple cracks. The specimen was cut along the line shown in Figs. 9(a) and 9(b), and the cross section was observed with the SEM. Note that the cutting line was located at the middle of the crack with the length $2a$ of 316 μm shown in Fig. 9(b). The crack plane was almost normal to the loading direction. The depth of the crack was 102 μm, and its aspect ratio b/a was 0.32. According to previous reports [29-32], large cracks tend to exhibit small aspect ratios,

with the aspect ratio of a long crack being around 0.3. This happens because the crack length drastically increases, while its depth does not change when cracks coalesce. Hence, this crack seemed to be formed due to the coalescence of several micro-cracks.

Figure 10 shows the number of cracks and maximum crack length as functions of testing time. As shown in Figs. 7 and 8, cracks first occurred at 145 min, and the number of cracks increased with testing time. After a testing time of 720 min, the initiation and growth of cracks stopped. Note that the maximum crack length rapidly increased due to crack growth by the coalescence of neighboring cracks at around 160 min, and the number of cracks decreased due to the coalescence of cracks.

Figure 11 shows the histogram of the number of cracks versus crack length. At a testing time of 145 min, all cracks were less than 100 μm long. At 360 min, the number of cracks increased, and cracks longer than the average grain size were observed. Then, at 720 min, the number of cracks increased again, and several cracks longer than the grain size were formed. The number of cracks 150-200 μm long decreased from 360 min to 720 min because cracks coalesced.

3.2 Factors influencing SCC

Figure 12 shows the crystal orientation map with crack profile for the observation area shown in Figs. 7, 8, and 9. Fine and thick lines denote GBs and cracked GBs, respectively. Because all cracks were formed along GBs, we can conclude that IGSCC occurred during this experiment. In this section, we describe our investigation of the influence of GB structure, GB length, and stresses acting on GBs on intergranular crack initiation sites. Note that, for the sake of simplicity, we only focused on the presence or absence of cracks at GBs and did not consider crack formation process.

Table 4 shows the influence of susceptibility to IGSCC on GB structure. The table lists the number of GBs and cracked GBs in the observation area for three specimens. Σ3 and random boundaries occupied most of the GBs in all specimens. As for low-angle GBs, around 1% of these GBs were cracked, and these GBs exhibited susceptibility to SCC. As for CLS boundaries in high-angle GBs, several CLS boundaries were cracked. Regarding Σ3 boundaries, only three boundaries were cracked among thousands of Σ3 boundaries. As shown in Fig. 1, although a Σ3 boundary with a plane of {1 1 1} exhibits very high IGC resistance, the Σ3 boundaries with other planes – {1 1 0}, {2 1 1}, {2 1 0}, and {3 1 1} – exhibit little IGC resistance. To investigate the

susceptibility of Σ3 boundaries to SCC in detail, the plane of each cracked Σ3 boundary was identified based on the GB trace analysis proposed in the previous study [12]. Figure 13 shows the resulting SEM micrograph and crystal orientation map. The trace angle θ of the cracked Σ3 boundary was measured to be 50°, and the plane of the Σ3 boundary was identified as {2 1 0}. In fact, we could not find a cracked Σ3 boundary with a {1 1 1} plane. Thus, we can conclude that a Σ3 boundary with {1 1 1} also exhibits high resistance to SCC, while Σ3 boundaries with other planes exhibit susceptibility to SCC.

For other CLS boundaries, a few were cracked. Note that it was difficult to clarify the susceptibility of each CLS boundary to SCC because few of them were seen in the observation area. For random boundaries, several percent of these boundaries were cracked, and this boundary type exhibited susceptibility to SCC. We concluded that the trend in the susceptibility of GBs to SCC agreed with that for IGC. That is, SCC did not occur at the GBs with high IGC resistance, such as the Σ3 boundary with {1 1 1}. Instead, SCC occurred at the GBs with little IGC resistance. Note that SCC occurred at most in a few tens of percent of the GBs with little IGC resistance, and the condition that the GB structure which had susceptibility to IGC was a necessary condition for the occurrence of IGSCC.

Figure 14(a) shows the histogram of the number of GBs versus crack length. Note that the GB length of the Σ3 boundary was not included in this figure because few cracked Σ3 boundaries were observed. The bars and scatter bars denote the average, maximum, and minimum values in the three specimens. Among all GBs, the GBs with a length of less than 20 μm were most common, and the number of GBs decreased with increasing GB length. Among cracked GBs, the numbers with lengths from 20 μm to 40 μm were the largest, but the number decreased with GB length above and below this range. To investigate the relationship between GB length and IGSCC, the probability of n_c/n_{all} as a function of GB length was replotted as shown in Fig. 14(b). The probability increased with increasing GB length, and it was found that a longer GB exhibited higher susceptibility to SCC. A similar behavior of IGSCC was previously reported by Kako et al. [33].

Figure 15 shows the histogram of the number of GBs and cracked GBs versus the normalized effective stresses of $\sigma_N/\sigma_{0.2}$ and $\tau_N/\sigma_{0.2}$ acting on GBs. Again, we omitted the results for the Σ3 boundaries. The bars and scatter bars denote the average, maximum, and minimum values in the

three specimens. The distribution of effective normal stress for all GBs was different from that for cracked GBs. The distribution of effective shear stress for all GBs agreed with that for cracked GBs. Hence, it seemed that normal stress affected the nucleation of IGSCC, but shear stress had little effect. To evaluate the relationship between normal stress, shear stress, and IGSCC, the probability of n_c/n_{all} as a function of normalized effective stresses of $\sigma_N/\sigma_{0.2}$ and $\tau_N/\sigma_{0.2}$ was replotted as Fig. 16. The probability increased with increasing effective normal stress, while the probability was approximately constant for all effective shear stress values. We concluded that SCC preferentially occurs at GBs subjected to high normal stress, and that shear stress does not affect the occurrence of IGSCC.

3.3 Criterion for initiation of IGSCC

In Sec. 3.2, factors influencing IGSCC were investigated. From a crystallographic viewpoint, the structure that made GBs susceptible to SCC corresponded to the structures that made GBs susceptible to IGC, and the SCC tended to occur at long GBs. From a mechanical viewpoint, SCC preferentially occurred at GBs subjected to high normal stress. As mentioned in the introduction, the susceptibility of SCC depends on material, environment, and stress. Hence, a criterion for initiation of IGSCC could be formulated based on several influencing factors, that is, the GB structure, GB length, and stresses acting on GBs.

From a mechanical viewpoint, we propose a criterion for microscopic intergranular cracking in polycrystalline materials based on the GB length and stresses acting on the GBs [34-37]:

$$l \cdot (\sigma^2 + \tau^2) = \beta K_{CB}^2 \, (= const.), \tag{10}$$

where l, σ, τ, β, and K_{CB} are GB length, normal stress acting on a GB, shear stress acting on a GB, a constant, and fracture toughness of a GB, respectively. Although shear stress acting on GBs would not affect the nucleation of IGSCC, as mentioned in Sec. 3.2, we decided to apply eq. (10) to the intergranular crack initiation in this study for the sake of simplicity. From a crystallographic viewpoint, the normalized width of IGC, w' (=w/w_{rand} in Fig. 1), was applied to eq. (10). As a result, the crack initiation was evaluated based on the combination of $w' \cdot l \cdot (\sigma_N^2 + \tau_N^2)$ from crystallographic and mechanical viewpoints. Note that the values of w' were beyond unity at several CSL boundaries because the normalized width of IGC exhibited large scatter. Hence, the upper bound of w' was set to

be unity to ignore the experimental scatter because random boundaries are expected to have the highest susceptibility to SCC.

Figure 17 shows the probability of IGSCC (n_c/n_{all}) as a function of the value of $w' \cdot l \cdot (\sigma_N^2+\tau_N^2)$. The bar and scatter bars denote the average, maximum, and minimum values in the three specimens. When the value of $w' \cdot l \cdot (\sigma_N^2+\tau_N^2)$ was less than 4 MPa^2·m, the probability was less than 10%. However, when the value of $w' \cdot l \cdot (\sigma_N^2+\tau_N^2)$ was more than 4 MPa^2·m, the probability became more than 25%. This implied that GBs with $w' \cdot l \cdot (\sigma_N^2+\tau_N^2) > 4$ MPa^2·m cracked preferentially, and this criterion was effective for evaluating the initiation of IGSCC.

3.4 Ways to improve the criterion

The criterion proposed in this study could approximately evaluate the susceptibility of GBs to SCC from the viewpoints of various influences. However, the evaluation based on this criterion exhibited a little scatter, as shown in Fig. 17: the probability was more than 40% when $w' \cdot l \cdot (\sigma_N^2+\tau_N^2) > 4$ MPa^2·m for a certain specimen, although the probability was around 20% under same conditions in other specimens. To improve the criterion, it is necessary to clarify the influencing factors in more detail.

As for the mechanical factor, inaccuracies in evaluating the stresses acting on GBs were caused by two reasons. First, we used the SMGBS model, which calculates stress based on the Schmid factors of neighboring grains with an assumption that steel is an elastic–fully plastic body. Because the experiment avoided destructive evaluation, the tilt angle ϕ in eq. (3) was assumed to be 90°, which might be inaccurate. If the angle ϕ could be measured, it would be possible to evaluate the stresses acting on GBs based on the SMGBS model. Stratulat et al. [24] cut a trench across GBs after IGSCC testing with a focused ion beam to accurately measure the tilt angle ϕ to evaluate the influence of normal stress during IGSCC based on the SMGBS model. In this study, we focused on the IGSCC behavior at thousands of GBs, and it was impractical to measure their tilt angle by the same technique. Moreover, the SMGBS model was too simple to calculate accurate stresses acting on GBs in a polycrystalline material. Mochizuki and Mikami [38] conducted crystal plasticity finite element analysis to calculate accurate stresses for the investigation on intergranular crack initiation. Second, the redistribution of stresses due to crack initiation, propagation, and coalescence was

ignored. When a crack is initiated near a GB, stresses acting on the GB change. In this study, stresses acting on GBs were calculated by the SMGBS model, which does not account for the redistribution of stresses; therefore, the stresses acting on cracked GBs due to crack growth and/or coalescence would be incorrect. Several techniques are available for determining the stresses acting on GBs, including crystal plasticity finite element method, which accounts for crack initiation; growth and coalescence measurement; and in situ measurement of microscopic stresses acting at each grain [39] during testing. Recently, Radchenko et al. [40] and Chen et al. [41] proposed a polychromatic X-ray microdiffraction technique to study a crystalline structure and its evolution in materials with a micrometer spatial resolution. Chao et al. [42, 43] evaluated the microscopic strain distributions in the vicinity of stress corrosion cracks using the X-ray microdiffraction technique. They clarified that a stress corrosion crack grew along a GB subjected to tensile strain. It is expected that mechanical factors which influence SCC nucleation on a smooth surface are clarified if microscopic stresses/strains at a GB just before cracking are measured by the X-ray microdiffraction technique.

With regard to crystallographic factors, the use of the Σ value measured by EBSD is insufficient for evaluating IGC susceptibility because the stability of GBs cannot be evaluated based only on the Σ value [11, 12]. A parameter that can characterize the structure of GBs as a measure of GB stability should be considered. As for the combination of these influencing factors, the formulation format needs to be optimized.

We evaluated the nucleation of IGSCC under accelerated conditions by using sensitized stainless steel and a corrosive solution, and it is impossible to directly apply the obtained results to actual problems that occur in nuclear power plants and chemical plants. To use the criterion in practical applications, the influencing factors related to stress must be evaluated based on the crack initiation data obtained under actual conditions. Thus, more investigations for improvement of the criterion are necessary.

4. Conclusions

IGSCC testing was conducted on sensitized type 304 austenitic stainless steel in a tetrathionate solution. The conditions of initiation of IGSCC on a smooth surface were discussed from crystallographic and mechanical viewpoints. The character and length of GBs were determined

using crystal orientation map analyzed by EBSD, and the stresses acting on GBs were calculated by the SMGBS model. The following conclusions were obtained:

1. Many grain-sized cracks occurred along GBs after the incubation time, and then the cracks multiplied and lengthened due to crack growth and coalescence.
2. Regarding the influence of GB structure on SCC, it occurred at GBs with little IGC resistance, such as random boundaries, while SCC did not occur at GBs with high IGC resistance, such as Σ3 boundaries with a {1 1 1} plane. Regarding geometry, long GBs exhibited high susceptibility to SCC. Regarding the influence of stresses acting on GBs, SCC preferentially occurred at GBs subjected to high normal stress.
3. A criterion for IGSCC was developed based on the susceptibility of GBs to IGC, the length of GBs, and the normal and shear stresses acting on GBs. The criterion could approximately investigate GBs at which SCC preferentially occurred.

Acknowledgments

The present work was supported by JSPS KAKENHI Grant Numbers JP26420011 and 17H04899; the Inamori Foundation; and Hitachi Metals / Materials Science Foundation.

References

[1] ISO 15510: 2014, Stainless steels - Chemical composition.

[2] IAEA, IAEA Nuclear Energy Series No. NP-T-3.13, Stress Corrosion Cracking in Light Water Reactors: Good Practices and Lessons Learned, (2011), pp. 18-37.

[3] M. Nakahara, Preventing Stress-Corrosion Cracking of Austenitic Stainless Steels in Chemical Plants, NiDI Technical Series No. 10066, (1992).D

[4] A.Y. Kina, V.M. Souza, S.S.M. Tavares, J.M. Pardal and J.A. Souza, Microstructure and intergranular corrosion resistance evaluation of AISI 304 steel for high temperature service, Materials Characterization, Vol. 59 (2008), pp.651-655.

[5] S.-X. Li, Y.-N. He, S.-R. Yu, and P.-Y Zhang, Evaluation of the effect of grain size on chromium carbide precipitation and intergranular corrosion of 316L stainless steel, Corrosion Science, Vol. 66 (2013), pp. 211-216.

[6] L.S. Shvindlerman and B.B. Straumal, Regions of existence of special and non-special grain boundaries, Acta Metallurgica, Vol. 33(1985), pp. 1735-1749.

[7] M. Shimada, H. Kokawa, Z.J. Wang, Y.S. Sato, and I. Karibe, Optimization of grain boundary character distribution for intergranular corrosion resistant 304 stainless steel by twin-induced grain boundary engineering, Acta Materialia, Vol. 50 (2002), pp. 2331-2341.

[8] C. Hu, S. Xia, H. Li, T. Liu, B. Zhou, W. Chen, and N. Wang, Improving the intergranular corrosion resistance of 304 stainless steel by grain boundary network control, Corrosion Science Vol. 53 (2011) pp. 1880-1886.

[9] S. Kobayashi, R. Kobayashi, and T. Watanabe, Control of grain boundary connectivity based on fractal analysis for improvement of intergranular corrosion resistance in SUS316L austenitic stainless steel, Acta Materialia, Vol. 102 (2016), pp. 397-405.Hu et al. [8],

[10] C.M. Barr, S. Thomas, J.L. Hart, W. Harlow, E. Anber, and M.L. Taheri, Tracking the evolution of intergranular corrosion through twin-related domains in grain boundary networks, npj Materials Degradation, Vol. 2 (2018), Article number: 14.

[11] T. Haruna, T. Shimizu, and M. Kamaya, Correlation between grain boundary character and susceptibility of sensitization for SUS304 stainless steel foil with coarse grained structure, Journal of the Japan Institute of Metals, Vol. 76 (2012), pp. 314-320.

[12] T. Fujii, K. Tohgo, Y. Mori, and Y. Shimamura, Crystallography of intergranular corrosion in sensitized austenitic stainless steel, Materials Characterization, Vol. 144 (2018), pp.219-226.

[13] P. L. Andresen and M. M. Morra, IGSCC of non-sensitized stainless steels in high temperature water, Journal of Nuclear Materials, Vol. 383 (2008), pp.97-111.

[14] T. Terachi, T. Yamada, T. Miyamoto, K. Arioka, SCC growth behaviors of austenitic stainless steels in simulated PWR primary water, Journal of Nuclear Materials, Vol. 426 (2012), pp. 59-70.

[15] T. Fujii, K. Tohgo, N. Ishizuka, Y. Shimamura, M. Takanashi, Y. Itabashi, G. Nakayama, Y. Sakakibara, and T. Hirano, Fracture mechanics study on stress corrosion cracking behavior under corrosive environment, Journal of Solid Mechanics and Materials Engineering, Vol. 7(3) (2013), pp. 341-356.

[16] K. Saito and J. Kuniya, Mechanochemical model to predict stress corrosion crack growth of stainless steel in high temperature water, Corrosion Science, Vol. 43 (2001), pp. 1751-1766.

[17] T. Shoji, Z. Lu, H. and Murakami, Formulating stress corrosion cracking growth rates by combination of crack tip mechanics and crack tip oxidation kinetics, Corrosion Science, Vol. 52 (2010), pp. 769-779.

[18] P.L. Andresen and M.M. Morra, Effect of rising and falling *K* profiles on SCC growth rates in high-temperature water, Journal of Pressure Vessel Technology, Vol. 129 (2006), pp. 488-506.

[19] K Chen, J. Wang, D. Du, P.L. Andresen, and L. Zhang, d*K*/d*a* effects on the SCC growth rates of nickel base alloys in high temperature water, Journal of Nuclear Materials, Vol. 503 (2018), pp. 13-21.

[20] T. Fujii, K. Tohgo, M. Kawamori, and Y. Shimamura, Characterization of stress corrosion crack growth in austenitic stainless steel under variable loading in small- and large-scale yielding conditions, Engineering Fracture Mechanics, Vol. 205 (2019), pp.94-107.

[21] V. Y. Gertsman and S. M. Bruemmer, Study of grain boundary character along intergranular stress corrosion crack paths in austenitic alloys, Acta Materialia, Vol. 49 (2001), pp. 1589-1598.

[22] E.A. West, and G.S. Was, A model for the normal stress dependence of intergranular cracking of irradiated 316L stainless steel in supercritical water, Journal of Nuclear Materials, Vol. 408 (2011) , pp. 142-152.

[23] E.A. West, and G.S. Was, Strain incompatibilities and their role in intergranular cracking of irradiated 316L stainless steel, Journal of Nuclear Materials, Vol. 441 (2013) , pp. 623-632.

[24] A. Stratulat, J.A. Duff, and T.J. Marrow, Grain boundary structure and intergranular stress corrosion crack initiation in high temperature water of a thermally sensitised austenitic stainless steel, observed in situ, Corrosion Science, Vol.85 (2014), pp. 428-435.

[25] T. Liu, S. Xia, Q. Bai, B. Zhou, L. Zhang, Y. Lu, and T. Shoji, Three-dimensional study of grain boundary engineering effects on intergranular stress corrosion cracking of 316 stainless steel in high temperature water, Journal of Nuclear Materials, Vol. 498 (2018), pp. 290-299.

[26] S.A. Shipilov, Solving some key failure analysis problems using advanced methods for materials testing, Engineering Failure Analysis, Vol.14 (2007), 1550-1573.

[27] D.G. Brandon, The structure of high-angle grain boundaries, Acta Metallurgica, Vol. 14 (1966), pp. 1479-1484.

[28] E. Schmid and W. Boas, Plasticity of Crystals, Hughes & Co., London (1950).

[29] M. Kamaya and T. Haruna, Influence of local stress on initiation behavior of stress corrosion cracking for sensitized 304 stainless steel, Corrosion Science, Vol. 49 (2007), pp.3303-3324.

[30] M. Akashi and T. Kawamoto, Intergranular stress corrosion crack propagation behavior of sensitized stainless steels in high temperature pure water, Boshoku Gijyutsu, Vol. 32 (1983), 9-15.

[31] K. Tohgo, H. Suzuki, Y. Shimamura, G. Nakayama, and T. Hirano, Monte Carlo simulation of stress corrosion cracking on a smooth surface of sensitized stainless steel type 304, Corrosion Science, Vol. 51 (2009), pp. 2208-2217.

[32] T. Fujii, K. Tohgo, A. Kenmochi, and Y. Shimamura, Experimental and numerical investigation of stress corrosion cracking of sensitized type 304 stainless steel under high-temperature and high-purity water, Corrosion Science, Vol. 97 (2015), pp.139-149.

[33] K. Kako, et al. Effect of grain size on stress corrosion cracking of austenitic stainless steel in high temperature water, Denryoku Chuo Kenkyusho Hokoku (no.Q08022) ISSN 1340-4652 (2009) 1-4, 1-17.

[34] A.G. Evans, Microfracture from thermal expansion anisotropy – I. Single phase system, Acta Metallurgica, Vol. 26 (1978), pp. 1845-1853.

[35] N. Laws and J.C. Lee, Microcracking in polycrystalline ceramics: Elastic isotropy and thermal anisotropy, Journal of the Mechanics and Physics of Solids, Vol. 37 (1989), pp. 603-618.

[36] B. Kim, H. Naitoh, S. Wakayama and M. Kawahara, Simulation of microfracture process and fracture strength in 2-dimensional polycrystalline materials", JSME international Journal, Series A, Vol. 39 (1996), pp. 548-554.

[37] T. Fujii, Y. Akiniwa, and T. Amata, Brittle fracture analysis of porous ceramics based on initiation of micro damages, Journal of the Society of Materials Science, Japan, Vol. 56 (2007), pp. 244-251.

[38] M. Mochizuki and Y. Mikami, Prediction of SCC initiation in weld components by multi-scale analysis incorporating crystal plasticity, Proceedings of the ASME 2010 Pressure Vessels and Piping Division/K-PVP Conference (PVP2010), 2010, pp. 189-195.

[39] K. Tanaka and Y. Akiniwa, The fundamental principles and techniques of X-ray stress measurement and current developments in the field II: Microstress and Macrostress, Journal of the Society of Materials Science, Japan, Vol. 47 (1998), pp. 1301-1307.

[40] I. Radchenko, S.K. Tippabhotla, N. Tamura, and A.S. Budiman, Probing phase transformations and microstructural evolutions at the small scales: synchrotron X-ray microdiffraction for advanced applications in 3D IC (integrated circuits) and solar PV (photovoltaic) devices, Journal of Electronic Materials, Vol. 45 (2016), pp. 6222-6232.

[41] X. Chen, C. Dejoie, T. Jiang, C. Ku, and N. Tamura, Quantitative microstructural imaging by scanning Laue x-ray micro- and nanodiffraction, MRS Bulletin, Vol. 41 (6) (2016), pp. 445-453.

[42] J. Chao, M.L.S. Fuller, N.S. McIntyre, A.G. Carcea, R.C. Newman, M. Kunz, and N. Tamura, The study of stress application and corrosion cracking on Ni-16 Cr-9 Fe (Alloy 600) C-ring samples by polychromatic X-ray microdiffraction, Acta Materialia, Vol. 60(3) (2012), pp. 781-792.

[43] J. Chao, M.L.S. Fuller, N. Sherry, J. Qin, N.S. McIntyre, J. Ulaganathan, A.G. Carcea, R.C. Newman, M. Kunz, and N. Tamura, Plastic and elastic strains in short and long cracks in Alloy 600 studied by polychromatic X-ray microdiffraction and electron backscatter diffraction. Acta Materialia, Vol. 60(15) (2012), pp. 5508-5515.

Figures

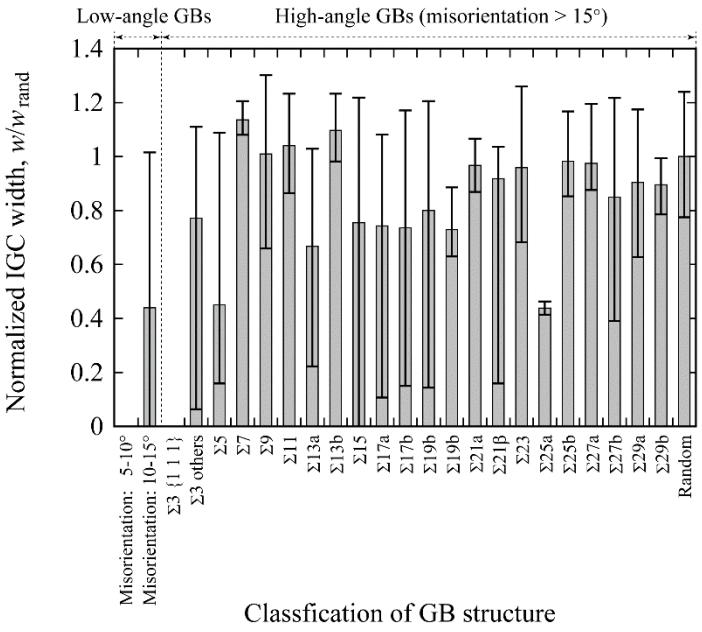

Fig. 1 Susceptibility of GB structure to intergranular corrosion [12].

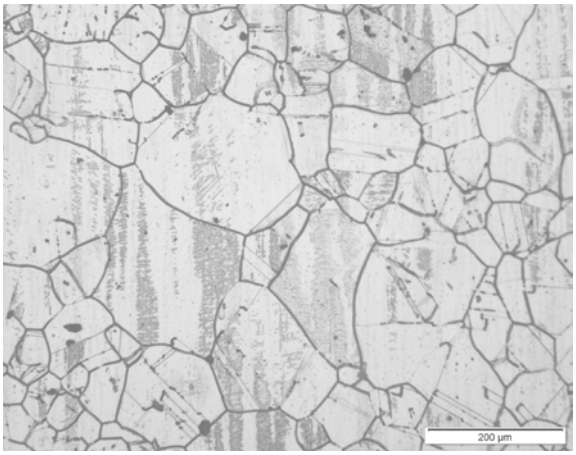

Fig. 2 Microstructure of the steel used in this study.

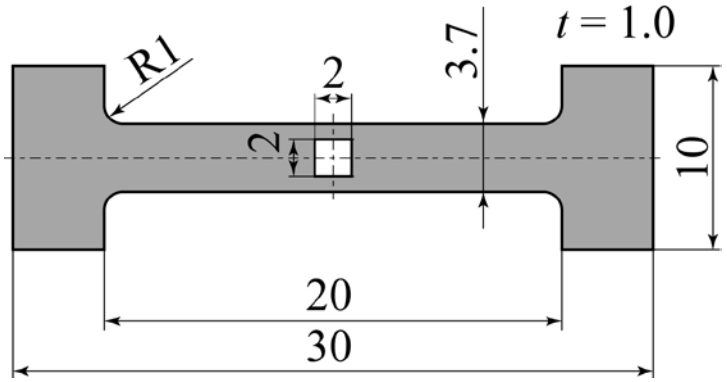

Fig. 3 Specimen dimensions (units = mm).

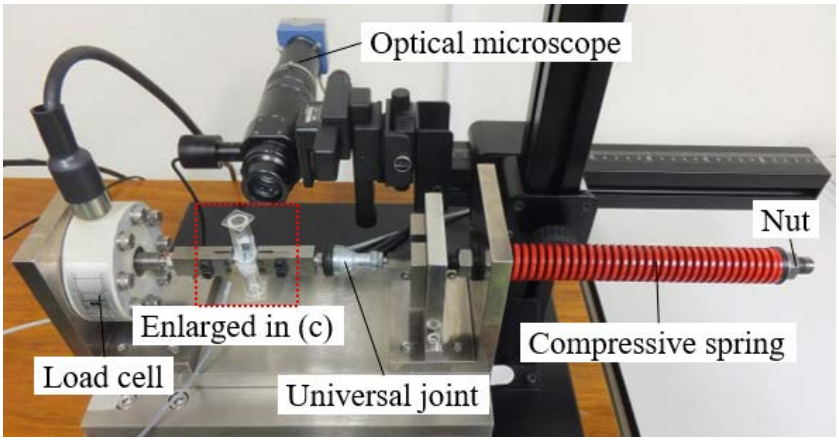

(a) Setup for constant load testing.

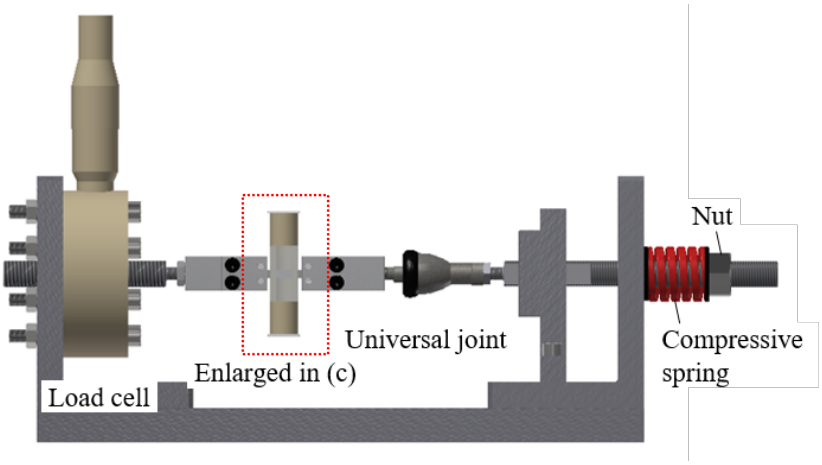

(b) Schematic illustration of constant load testing setup.

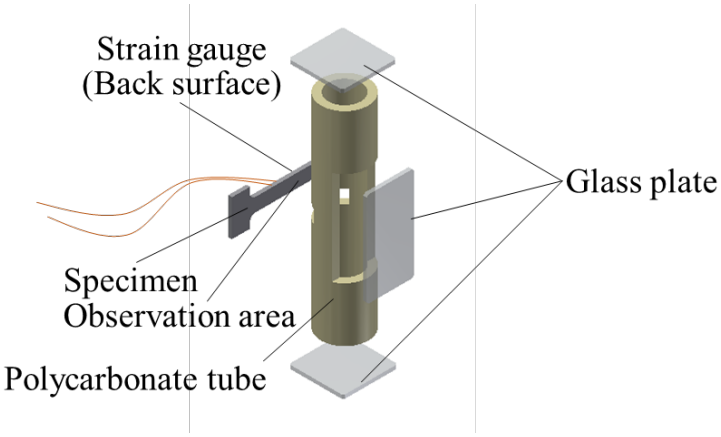

(c) Detail of specimen mount (red outline in panel (a)).

Fig. 4 Laboratory tensile testing apparatus.

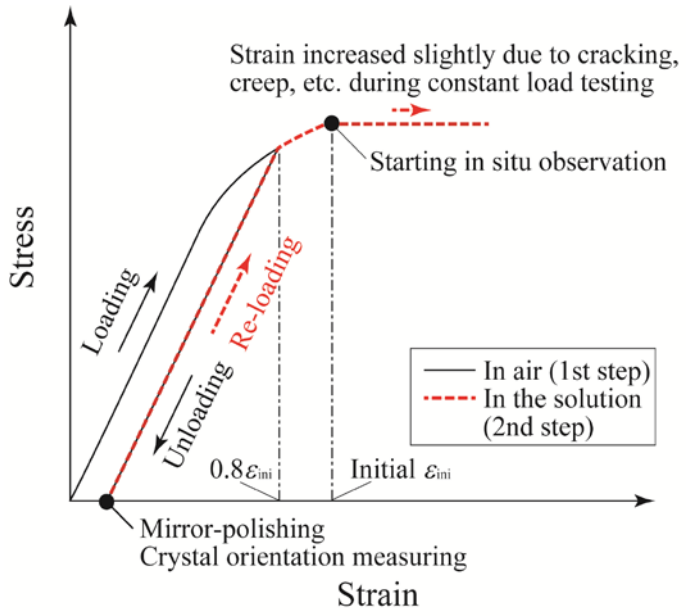

Fig. 5 Schematic of loading procedure (stress-strain curve).

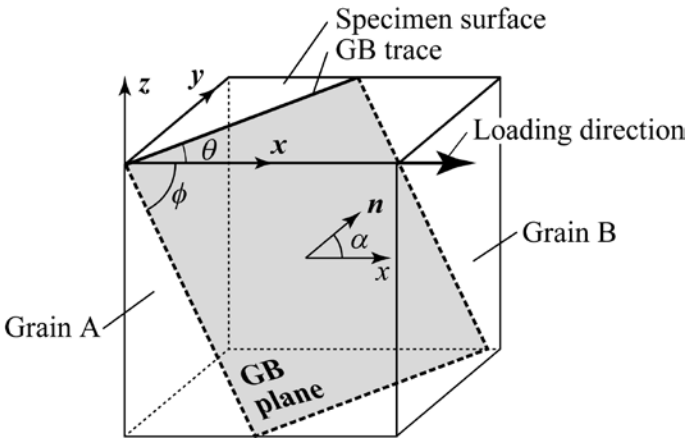

Fig. 6 Schematic of GB geometry in the SMGBS model. The vector ***n*** denotes the vector normal to the GB plane, and angle α denotes the angle between the tensile direction and normal direction in the GB plane.

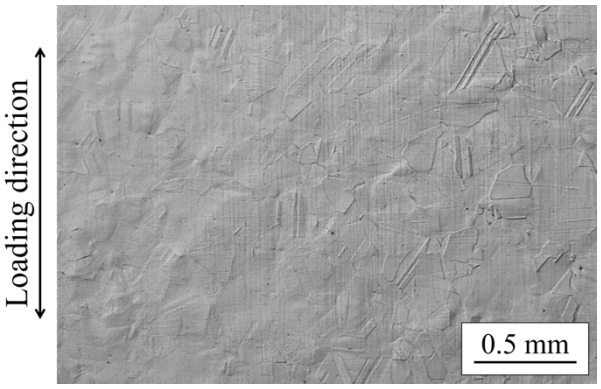

(a) 0 min.

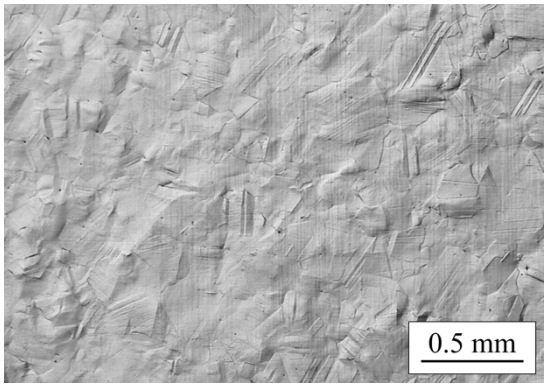

(b) 145 min.

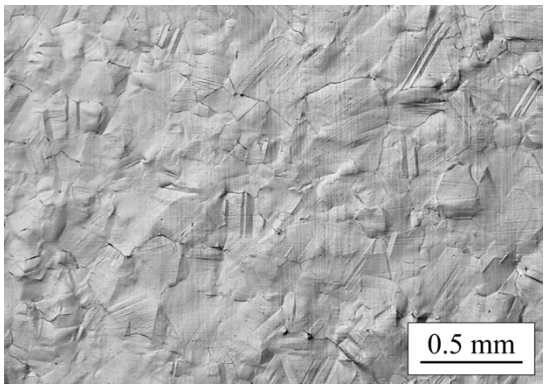

(c) 360 min.

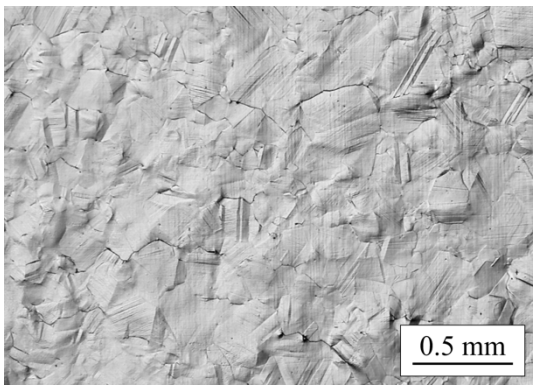

(d) 720 min.

Fig. 7 Cracking behavior during testing.

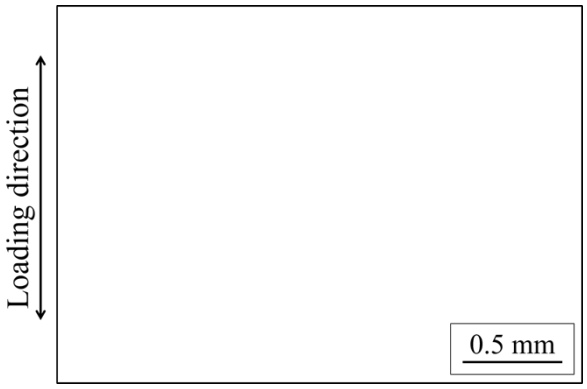

(a) 0 min.

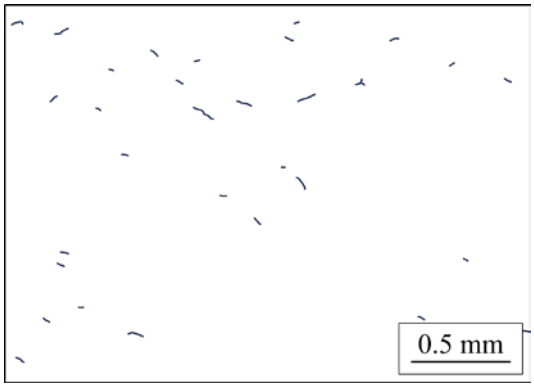

(b) 145 min.

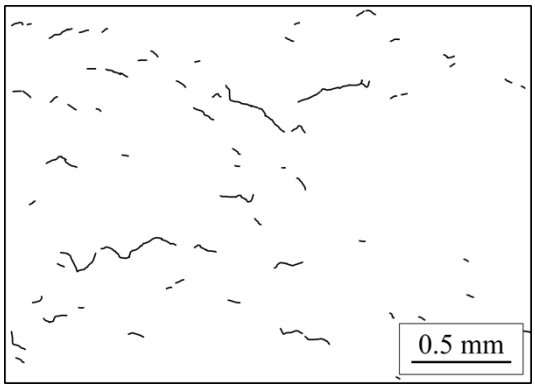

(c) 360 min.

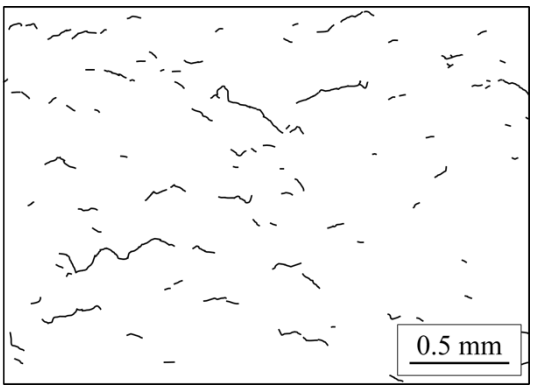

(d) 720 min.

Fig. 8 Schematics of crack profiles shown in Fig. 7.

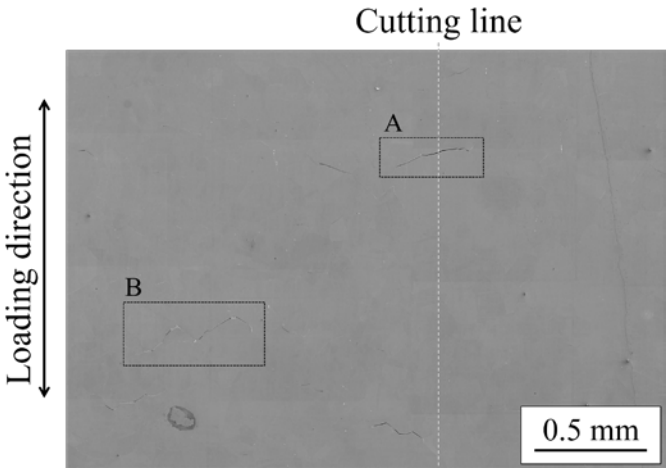

(a) Overall view.

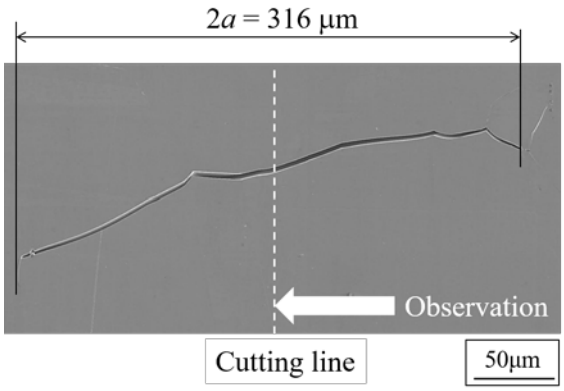

(b) Detail of area A in panel (a).

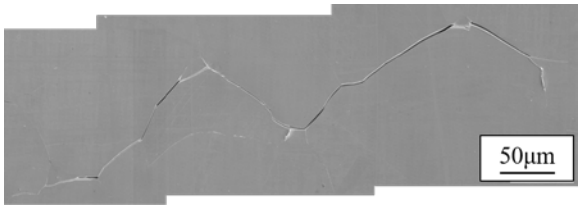

(c) Detail of area B in panel (a).

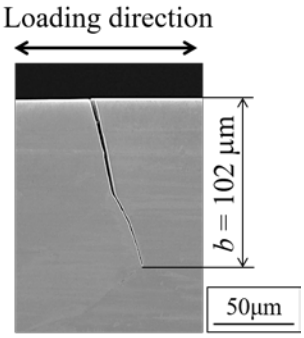

(d) Cross-section along the cutting line in panel (a).

Fig. 9 SEM micrographs of the specimen after testing. The values of 2*a* and *b* denote the crack length and depth, respectively.

Figures and tables 5

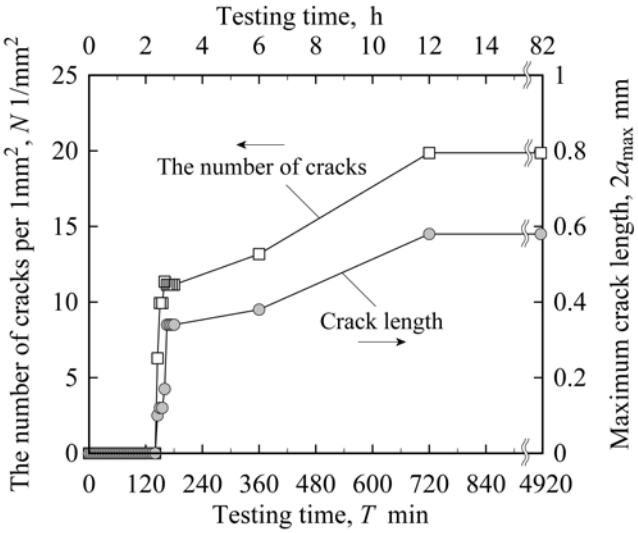

Fig. 10 Change in the number of cracks and maximum crack length during testing.

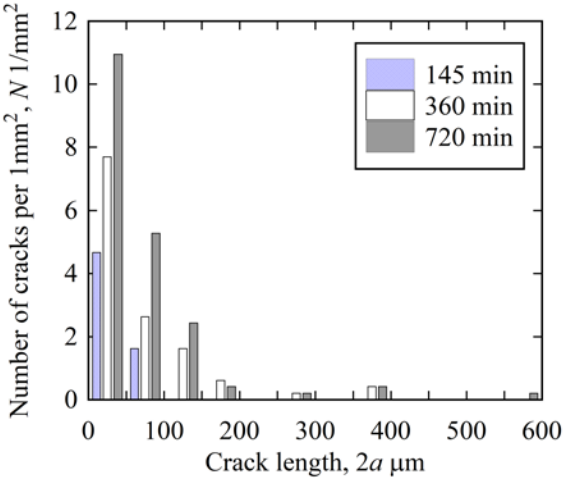

Fig. 11 Histogram of the number of cracks versus crack length.

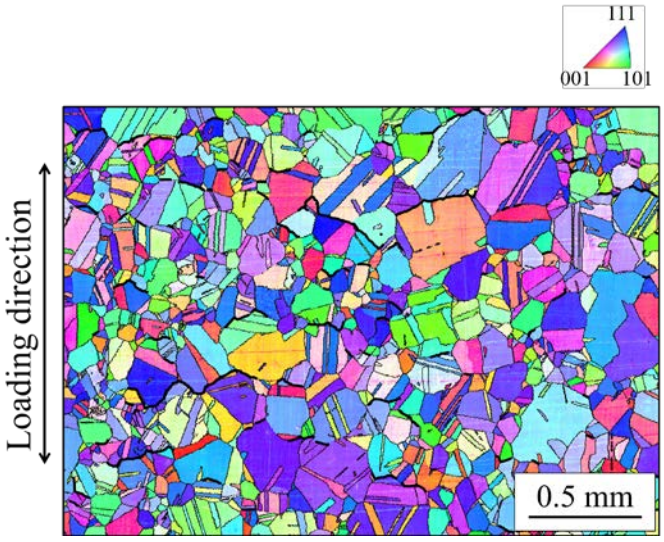

Fig. 12 Crystal orientation map with crack profile.

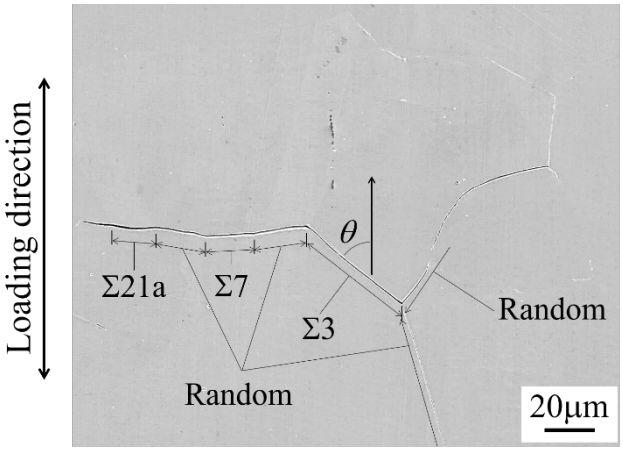

(a) SEM micrograph.

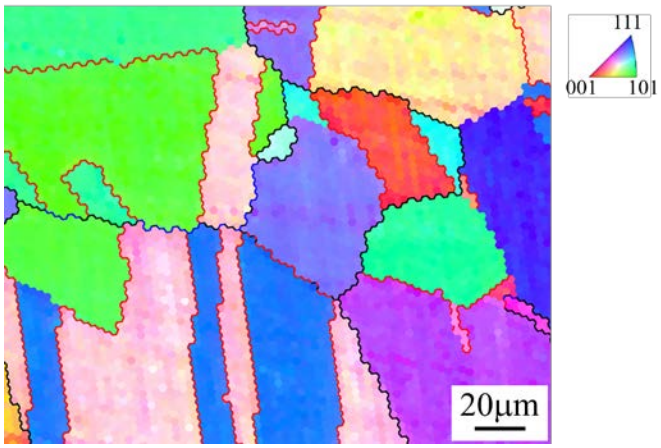

(b) Crystal orientation map corresponding to panel (a). Red, blue, and black lines denote Σ3 boundaries, other CLS boundaries (Σ5- Σ29b), and random boundaries, respectively.

Fig. 13 Intergranular stress corrosion cracking (IGSCC) at the Σ3 boundary

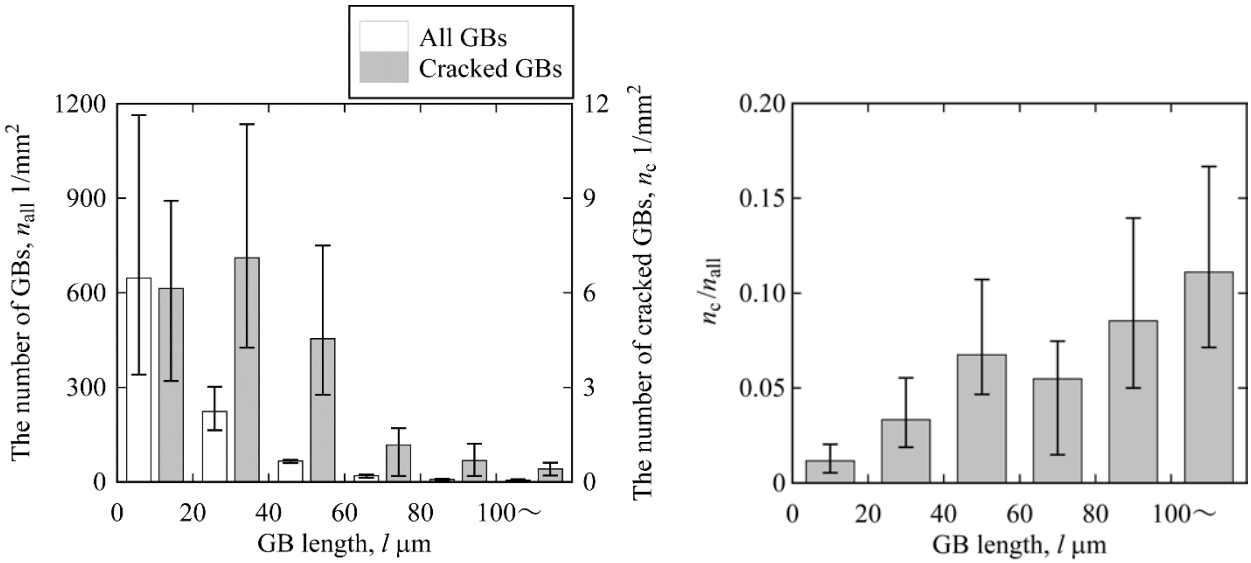

(a) Comparison of all GBs and cracked GBs. (b) Normalized distribution.

Fig. 14 Histograms of the number of cracks versus crack length.

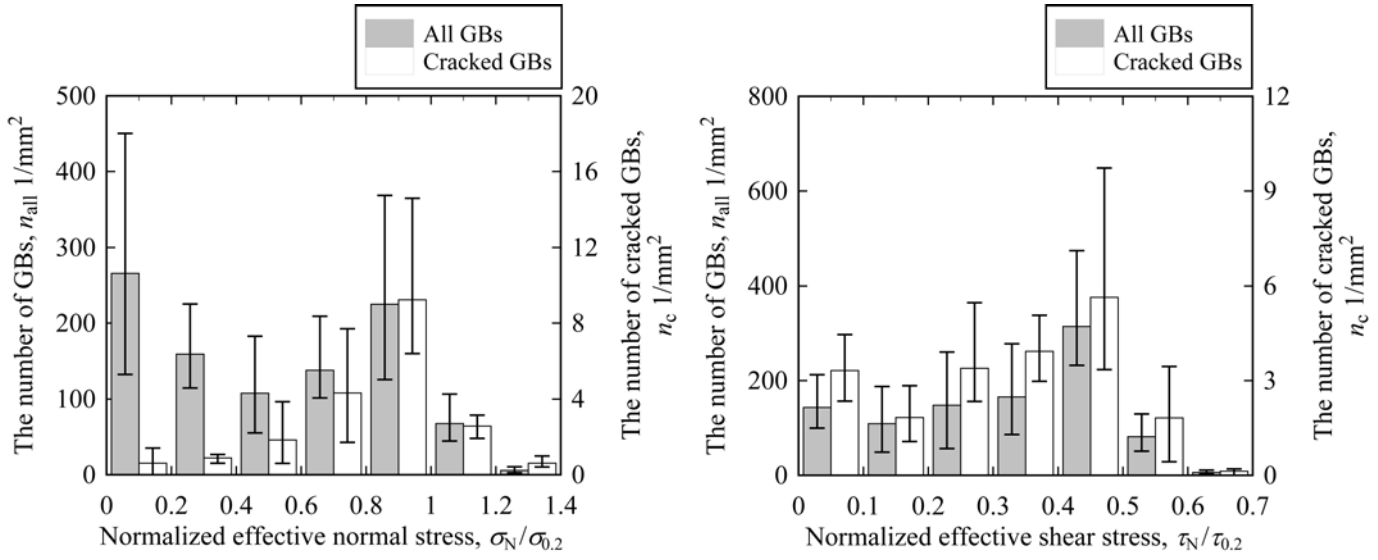

(a) Effective normal stress. (b) Effective shear stress.

Fig. 15 Influence of effective stresses on IGSCC.

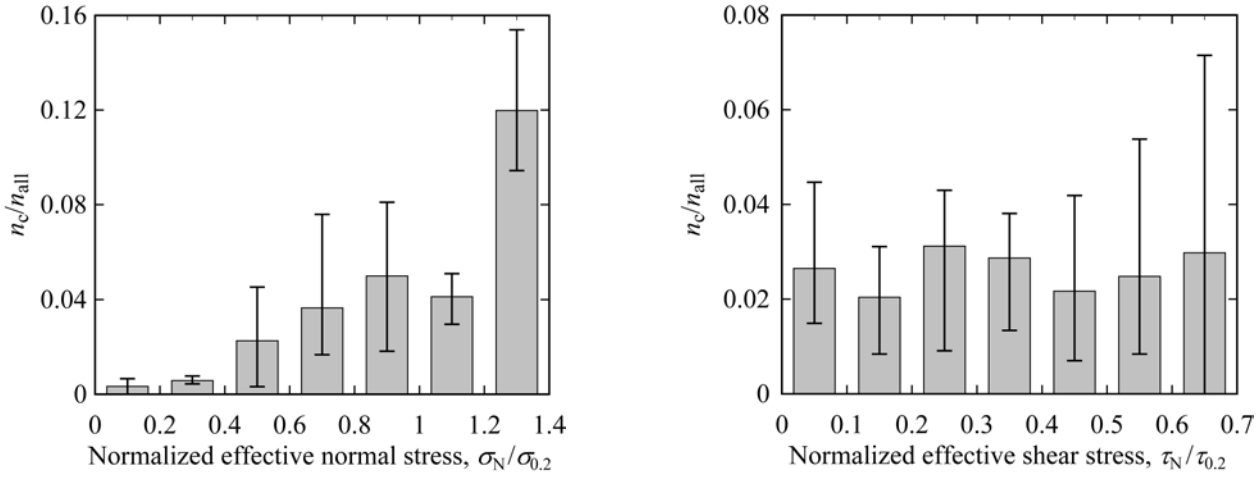

(a) Effective normal stress. (b) Effective shear stress.

Fig. 16 Probability of IGSCC occurring at GBs.

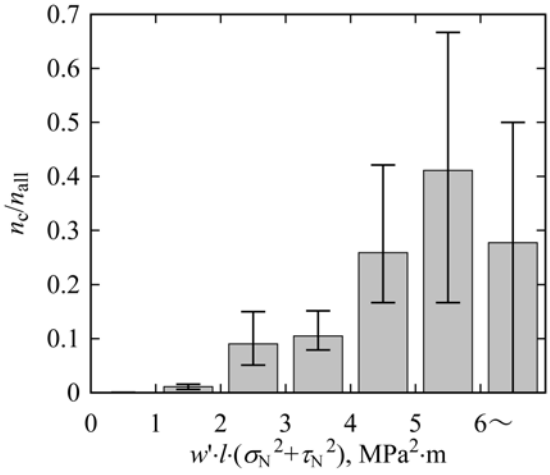

Fig. 17 Criterion for IGSCC nucleation.

Tables

Table 1 Chemical composition of steel used in this study (mass%).

C	Si	Mn	P	S	Ni	Cr	Fe
0.06	0.47	0.82	0.03	0.003	8.05	18.16	Bal.

Table 2 Mechanical properties of steel used in this study.

0.2% offset stress, MPa	Tensile strength, MPa	Elongation, %
206	520	40

Table 3 Conditions of EBSD measurement and analysis obtained by the OIM analysis.

Grid shape	Hexagonal
Measurement interval, μm	3.5
Grain tolerance angle, deg.	5
Minimum grain size, pixel	2
Clean up	Grain dilation, single iteration
Grain boundary length	Reconstructed boundaries
Boundary deviation	Two times step size

Table 4 Influence of IGSCC susceptibility on GB structure. The values n_{all} and n_c denote the numbers of GBs and cracked GBs, respectively, in the observation area of three specimens.

	GB class	Specimen 1			Specimen 2			Specimen 3			Summary of crack initiation
		n_{all}	n_c	n_c/n_{all} ×100, %	n_{all}	n_c	n_c/n_{all} ×100, %	n_{all}	n_c	n_c/n_{all} ×100, %	
Low-angle GBs	< 10°	107	0	0.00	145	0	0.00	81	1	1.23	Cracked
	10° - 15°	76	1	1.32	182	0	0.00	115	1	0.87	Cracked
High-angle GBs	Σ3	997	0	0.00	2892	0	0.00	1217	3	0.24	Cracked
	Σ5	17	0	0.00	65	0	0.00	2	0	0.00	
	Σ7	14	0	0.00	53	3	5.66	25	2	8.00	Cracked
	Σ9	99	1	1.01	262	1	0.38	93	2	2.15	Cracked
	Σ11	21	0	0.00	39	0	0.00	16	1	6.25	Cracked
	Σ13a	9	0	0.00	19	0	0.00	7	0	0.00	
	Σ13b	7	0	0.00	12	0	0.00	14	2	14.29	Cracked
	Σ15	12	0	0.00	29	0	0.00	23	1	4.35	Cracked
	Σ17a	7	0	0.00	1	0	0.00	4	0	0.00	
	Σ17b	7	1	14.29	19	1	5.26	9	1	11.11	Cracked
	Σ19a	12	0	0.00	21	0	0.00	7	0	0.00	
	Σ19b	6	0	0.00	15	0	0.00	6	0	0.00	
	Σ21a	6	1	16.67	13	0	0.00	6	2	33.33	Cracked
	Σ21b	12	0	0.00	16	0	0.00	12	3	25.00	Cracked
	Σ23	10	0	0.00	11	0	0.00	7	0	0.00	
	Σ25a	4	0	0.00	6	0	0.00	2	0	0.00	
	Σ25b	13	1	7.69	14	0	0.00	11	1	9.09	Cracked
	Σ27a	7	0	0.00	26	0	0.00	5	1	20.00	Cracked
	Σ27b	2	0	0.00	17	0	0.00	6	0	0.00	
	Σ29a	0	0	-	1	0	0.00	0	0	-	
	Σ29b	3	0	0.00	14	0	0.00	6	0	0.00	
	Random	2387	56	2.35	6923	76	1.10	3251	133	4.09	Cracked
Total		3835	61	-	10795	81	-	4929	154	-	-